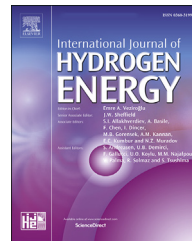




Available online at www.sciencedirect.com
ScienceDirect

journal homepage: www.elsevier.com/locate/he



Comprehensive study of deuterium-induced effects in austenitic stainless steel AISI 304L

Andreas Röhslér*, Oded Sobol, Wolfgang E.S. Unger, Thomas Böllinghaus

Bundesanstalt für Materialforschung und -prüfung, Unter den Eichen 87, 12205 Berlin, Germany

ARTICLE INFO

Article history:

Received 27 February 2019

Accepted 6 March 2019

Available online xxx

Keywords:

Hydrogen

Deuterium

AISI 304L

Martensite

ToF-SIMS

ABSTRACT

The damaging impact of hydrogen on the austenitic stainless steel AISI 304 L was analysed. To this aim, samples were charged electrochemically with the hydrogen isotope deuterium (^2H , D) and examined with time-of-flight secondary ion mass spectrometry (ToF-SIMS) and electron backscatter diffraction (EBSD). The fusion of the obtained chemical and structural information revealed local enrichment of deuterium in austenite, transformation into martensite, crack formation and severe roughening of the specimen surface. The results indicated that martensite was not only formed during charging but also during desorption and ToF-SIMS examinations. Furthermore, cross-sections of deuterium-charged samples revealed that in preferred deformation bands a $\gamma \rightarrow \epsilon \rightarrow \alpha'$ evolution is taking place.

By means of microscopic analyses and carrier gas hot extraction (CGHE), it was found that the use of NaAsO_2 as recombination poison decreased the uptake of hydrogen significantly and resulted in severe precipitation on the specimen surfaces. This is in contrast to the popular presumption that NaAsO_2 enhances the uptake of hydrogen (and deuterium) during electrochemical charging by hampering its recombination from atoms to molecules.

© 2019 The Author(s). Published by Elsevier Ltd on behalf of Hydrogen Energy Publications LLC. This is an open access article under the CC BY license (<http://creativecommons.org/licenses/by/4.0/>).

Introduction

Hydrogen-induced degradation of the mechanical properties of metals, commonly called hydrogen assisted cracking (HAC), is a phenomenon frequently occurring during transportation and storage of petrochemicals. Breakdown and failure of components in such infrastructures are frequently causing immense economical and ecological costs. As a result, engineers and scientists are facing major challenges to ensure the safe use of the applied structural elements.

Hydrogen can enter the microstructure during service and manufacturing processes like welding. It can drastically reduce its strength, toughness and ductility [1,2]. Through

accumulation of atomic hydrogen and its recombination to molecules, the matrix is strained and cracks can form also without external loads [3–5]. Głowacka et al. showed also that interstitial trapped hydrogen creates stress in $00\text{H}2\text{N}6$ duplex steel which leads to the nucleation of dislocations. It is known that the dislocations can then act as traps for hydrogen which in turn can induce more stresses in the lattice to form new dislocations [6,7].

In addition to dislocations and interstitial lattice sites as potential traps, also phase and grain boundaries, voids and precipitates are known to trap hydrogen [8–11].

The uptake and trapping of hydrogen can lead to hydrogen-assisted cracking (HAC) and loss of ductility [3,12,13]. In 1982, Minkovitz et al. already reported that

* Corresponding author.

E-mail address: andreas.roehsler@bam.de (A. Röhslér).

<https://doi.org/10.1016/j.ijhydene.2019.03.058>

0360-3199/© 2019 The Author(s). Published by Elsevier Ltd on behalf of Hydrogen Energy Publications LLC. This is an open access article under the CC BY license (<http://creativecommons.org/licenses/by/4.0/>).

Please cite this article as: Röhslér A et al., Comprehensive study of deuterium-induced effects in austenitic stainless steel AISI 304L, International Journal of Hydrogen Energy, <https://doi.org/10.1016/j.ijhydene.2019.03.058>

electrochemical hydrogen-charging of AISI 304 L led to the transformation of the face-centred cubic (FCC) matrix into body-centred tetragonal (BCT) α' -martensite [14]. Following this publication, other research groups showed by means of X-ray diffraction that the hexagonal close packed (HCP) ϵ -phase represents an intermediate stage of this transformation [3,15].

The brittle nature of martensite can be reflected by the reduction of the materials ductility and a change from transgranular ductile to intergranular brittle fracture mode [11,16,17]. Moreover, the hydrogen diffusion in martensite is faster than in austenite [18]. Thus, hydrogen can enter the lattice more easily and accelerates the degradation process.

The aim of the present study is to visualise typical features of hydrogen degradation such as blistering, cracking and phase transformation and to correlate the global hydrogen concentration to the local distribution around microstructural features.

To this end, samples have been charged with hydrogen, and the total amount of charged hydrogen has been measured using carrier gas hot extraction (CGHE). Structural and microstructural changes in the material were identified by electron backscatter diffraction (EBSD) in combination with surface imaging in scanning electron microscopy (SEM). The local distribution of hydrogen in the microstructure was determined with time-of-flight secondary ion mass spectrometry (ToF-SIMS), using deuterium as tracer.

Although ToF-SIMS is one of few techniques capable to achieving this, the characterisation of metastable alloys like AISI 304 L is not straightforward. It is known that ion bombardment can cause transformation of the surface layer into an amorphous form or a new crystalline phase [19]. Therefore, it is necessary to carefully control the sputter process. To enhance the depth of information and to correlate chemical and morphological features, SIMS data was processed with principal component analysis (PCA) and fused with the SEM images.

Experimental

Material and specimen preparation

Subject of the experiments was the austenitic stainless steel EN 1.4307 (AISI 304 L), purchased from thyssenkrupp Schulte GmbH (Essen, Germany). The material was cold rolled before annealing and air cooling, followed by pickling and a final rolling step to a thickness of 0.5 mm. The chemical composition, measured with an optical emission spectrometer spectrotest (SPECTRO Analytical Instruments GmbH, Kleve, Germany), is shown in Table 1.

Based on the Schaeffler-Diagram, the investigated steel should consist of 90% austenite and 10% ferrite [20].

For the ToF-SIMS, SEM and EBSD analyses, samples with the dimension of $10 \times 10 \times 0.5$ mm were cut out of a sheet by

electric discharge machining (EDM). Subsequently, the specimen have been ground with SiC papers down to 4000 grit and polished on the analysis side with 3, 1 μm and 0.25 μm diamond suspension for 5 min per step.

After charging, EBSD and ToF-SIMS analyses of the surfaces, the cross sections were analysed after cautiously cutting the samples in half with a diamond-studded wire. In order to protect the surface from damaging, specimen were electrochemically plated with thin layers of gold and nickel beforehand. The cross-section itself was polished the same way as the surface and analysed by EBSD.

Alternatively to the mechanical surface polishing electrolyte polishing was applied. Despite a high-quality surface and excellent EBSD patterns, it decreased the hydrogen/deuterium charging considerably which is in contrast to observations of e.g. Warrier et al. where a higher surface quality increased the uptake of hydrogen [21]. Furthermore, the applied electrolyte polishing produced a wavy specimen surface, which rendered subsequent ToF-SIMS investigations difficult.

Electrochemical charging

The use of deuterium as tracer for hydrogen was inevitable in the present study, because ToF-SIMS instrumentations can not distinguish between artificially introduced hydrogen and adsorbed, abundant hydrogen from the rest gas in the device. Samples were charged electrochemically for 24 and 48 h in a solution of 0.05 M D_2SO_4 diluted in high purity D_2O .

In comparison, another set of samples was charged with the addition of 0.01 M NaAsO_2 acting as a recombination poison.

A current density of 5 mA/cm² was chosen. To keep the solution oxygen-free, it was constantly purged during charging with high purity gaseous nitrogen.

Carrier gas hot extraction

The differences in the uptake of deuterium with and without the addition of NaAsO_2 were analysed with carrier gas hot extraction, using a G8 Galileo from Bruker AXS GmbH (Karlsruhe, Germany) equipped with the quadrupole mass spectrometer ESD 1000 from InProcess Instruments Gesellschaft für Prozessanalytik mbH (Bremen, Germany). The device was calibrated for the detection of hydrogen, therefore samples had to be charged for 24 and 48 h in 0.05 M H_2SO_4 instead of D_2SO_4 . It was done also with and without the addition of 0.01 M NaAsO_2 .

The sample was introduced into the analysis chamber at room temperature and heated to 673 K. This temperature was kept for 20 min, followed by heating to 1173 K and holding for another 20 min. A heating rate of 0.5 K/s was chosen in both cycles. In this approach, high purity nitrogen is acting as carrier gas for transporting the effusing hydrogen to the thermal conductivity detector.

Table 1 – Chemical composition of the investigated steel AISI 304 L.

Element	C	N	Cr	Ni	Mn	Si	P	S
wt.-%	0.027	0.053	18.38	8.21	1.54	0.48	0.029	0.004

Solubility and diffusivity of hydrogen and deuterium in steel are in the same order of magnitude [22]. However, the difference in size and behaviour must be taken into account when extrapolating the amount of deuterium based on data derived from CGHE. Based on the mass isotope effect, it is assumed that the relationship between diffusivity of hydrogen and deuterium is:

$$\frac{D_H}{D_D} = \sqrt{\frac{m_D}{m_H}}, \quad (1)$$

[23], where D_H and D_D are the diffusion coefficients of hydrogen and deuterium, respectively, and m_H and m_D are the respective masses of the isotopes. A simplified expression of Eq. (1) is given by San Marchi et al. [23]:

$$D_H = \sqrt{2} D_D. \quad (2)$$

Following this, the concentration of deuterium was then derived from the measured amount of hydrogen with:

$$x_D = \frac{x_H}{\sqrt{2}} \quad (3)$$

where x_D and x_H are the amount of deuterium and hydrogen, respectively (cf. 3.1).

Time-of-flight secondary ion mass spectrometry

In order to analyse the deuterium distribution after charging for 24 and 48 h a TOFSIMS IV (IONTOF GmbH, Münster, Germany) was used. The sample was cleaned with acetone and inserted in the load lock where it was cooled to approximately -100°C and constantly purged with dry nitrogen to prevent water condensation from the rest gas. Thereafter, the sample was transferred to the analysis chamber and further cooled to $\approx -135^\circ\text{C}$ in order to reduce the mobility of deuterium in the specimen.

Directly before ToF-SIMS analyses, the surface of the sample was sputtered for 2 min with 3 kV Cs^+ ions in order to remove contaminations and to enhance the secondary ion yield of deuterium [4,24].

The data was acquired using the collimated burst alignment mode (CBA) using a 25 kV Bi^+ ion beam, enabling a good spatial resolution down to 100 nm [25]. The region of interest (ROI) was scanned in a sawtooth mode with 512 by 512 pixels and one shot per pixel.

Data treatment and data fusion

Temperature and device instabilities required a shift correction of the raw image data. All peaks were normalised to the total ion intensity.

The fusion of SEM and SIMS data as well as the principal component analysis (PCA) were done with the software *ImageLab* by Epina Softwareentwicklungs- und Vertriebs-GmbH (Retz, Austria). The PCA was applied on the acquired SIMS image data to consider covariant features, such as deuterium fragments, which are bound to oxygen. Applying PCA revealed features like this and hence increased the information content significantly. The following peaks were selected for the principal component analysis: H^- , D^- , O^- , OH^- , OD^- , O_2^- , O_2H^- , O_2D^- , FeD^- , FeOD^- and NiOD^- .

Scaling of the data ahead of the PCA brought the noise level of all peaks to the same order of magnitude. Thus, variances of the signals became visible and peaks comparable. For more information on multivariate data analysis and PCA, the reader is referred to the literature, e.g. Refs. [26–28].

Scanning electron microscopy and electron backscatter diffraction

Scanning electron microscopy images have been either captured in a *Supra 40* or in a LEO 1530VP (Carl Zeiss GmbH, Oberkochen, Germany). For microstructure imaging forward and backscattered electron detectors below and above the phosphor screen of an EBSD detector e-Flash^{HR} (Bruker Nano, Berlin, Germany) have been used. In order to gain insight into the deuterium-induced phase and microstructure changes, both SEM imaging and EBSD mapping were done at the same area before and after charging with deuterium.

An acceleration voltage of 20 and 30 kV, respectively, was chosen for both SEM imaging and EBSD investigations. The higher acceleration voltage has been selected to increase the penetration depth and interaction volume of the beam in order to compensate the electrochemical charging-induced alteration of the steel surface. Due to that, the gathered information originated from deeper layers of the material, which were less damaged.

Results and discussion

Influence of recombination poison on the charging process

The computed amount of hydrogen and the derived amount of deuterium are shown in Table 2.

Peak 1 is the first desorption peak during heating to 673 K and peak 2 is the second maximum when heating to 1173 K. The peak at the lower temperature (peak 1) is assumed to represent reversible traps such as grain boundaries, ferrite or strain fields of dislocations [29]. Further heating introduces more energy into the sample, thus prompting also stronger traps, like vacancies and γ/α' -interfaces, to release hydrogen [30,31].

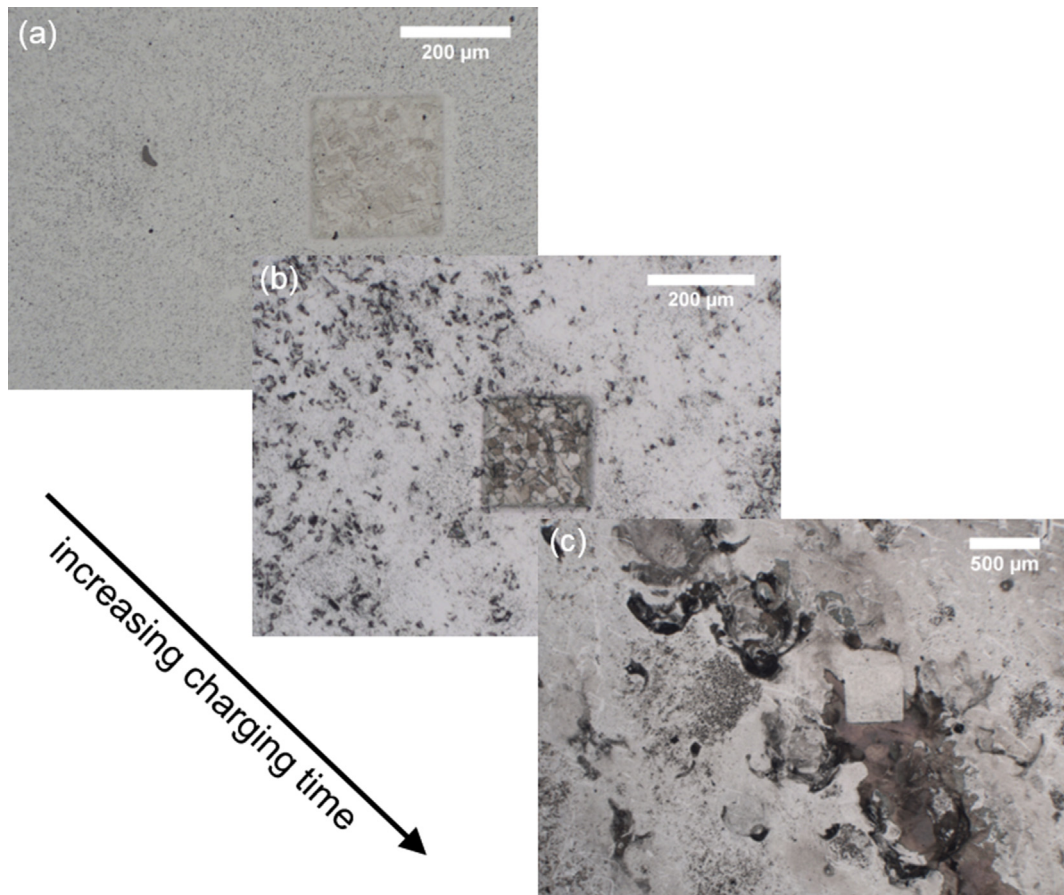
The results show that for both 24 and 48 h, the sample charged with NaAsO_2 contained less hydrogen than its respective counterpart. This is in contradiction to the experiences of other researchers who claim the utility as effective means to enhance the uptake of hydrogen by adding a recombination poison [3,13–15,32–35].

To obtain information about the chemical composition of the surface layer, ToF-SIMS investigations were conducted on other samples that were charged with addition of NaAsO_2 . Fig. 1 displays the specimen surface after charging for different times.

ToF-SIMS analyses showed that the surface layer contained arsenic, oxygen, iron, nickel, carbon, nitrogen and sulphur, while only a very few deuterium has been detected. Sputter times between 15 and 45 min were required until the intensity of the deuterium signal increased.

Table 2 – Calculated amount of hydrogen from the CGHE measurements, and estimated theoretical concentration of deuterium in steel after charging for 24 and 48 h, respectively.

[wt.-ppm]	with NaAsO ₂		without NaAsO ₂	
	measured x _H	estimated x _D	measured. x _H	estimated x _D
24 h	peak 1	13,3	9,4	31,8
	peak 2	3,1	2,2	3,4
	total	16,4	11,6	35,2
48 h	peak 1	62,6	44,3	84,3
	peak 2	1,4	0,9	1,8
	total	64,0	45,3	86,1

**Fig. 1 – Optical micrographs of samples charged for (a) 24, (b) 48 and (c) 72 h with 0.05 M D₂SO₄ + 0.01 M NaAsO₂. The square-shaped sputtered region of the ToF-SIMS examinations is clearly visible.**

Therefore, it is assumed that a certain amount of deuterium entered the matrix before the surface layer retarded the uptake of deuterium any deeper.

Phase transformation and microstructure changes

Figs. 2 and 3 show SEM images and EBSD maps of the same areas for samples before and after charging without the addition of NaAsO₂ for 24 and 48 h, respectively.

The specimen surface in 2(a) and 3(a) have been polished to mirror level. Within certain grains, twins are visible as parallel lines. This is due to local channeling-in behaviour of the

primary electron beam during scanning. After charging, the same areas exhibit a much higher roughness owing to the ingress of deuterium (cf. Figs. 2(b) and 3(b)). This is true except for a few grains which are smoother. In comparison to the phase maps in Figs. 2(d) and 3(c), it becomes clear that these areas have a BCC/BCT structure which existed already before charging and refer to α' -martensite. Although sample preparation by mechanical grinding and polishing was done with great care, martensitic transformation on the surface apparently occurred to a certain extent. In some cases entire austenite grains are changed near the surface to a thin martensite layer. Unlike this preparation-induced martensite,

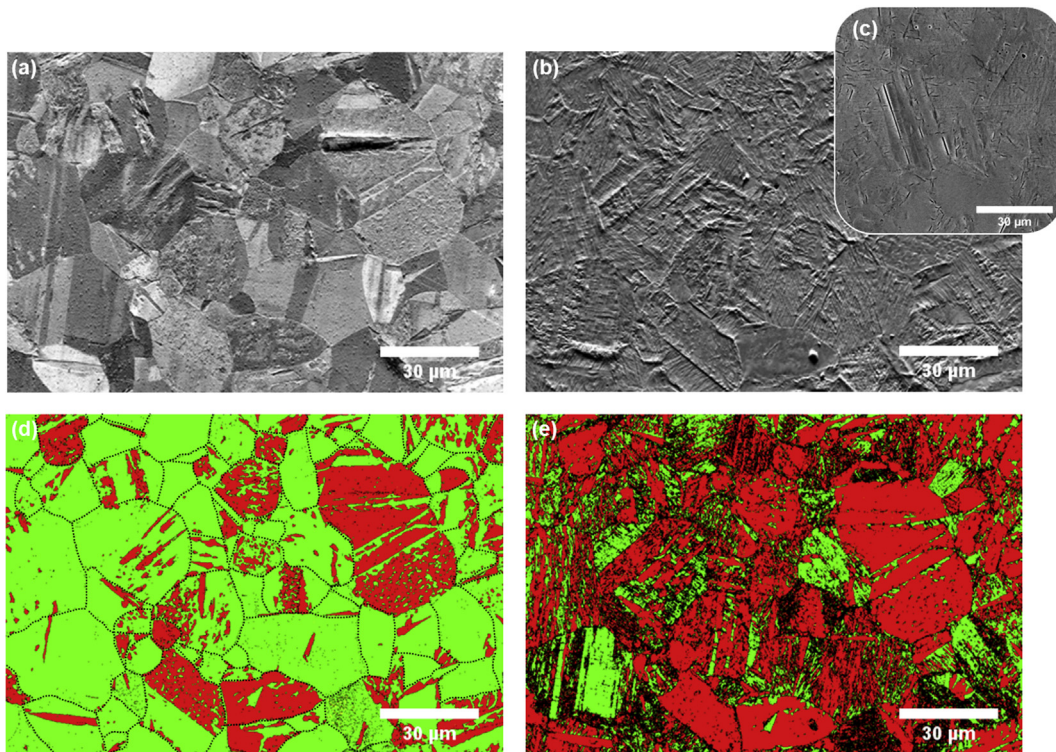


Fig. 2 – SEM images of the sample surface (a) before and (b)+(c) after electrochemical charging for 24 h. (c) represents a magnified area of (b). The respective phase distribution maps are displayed in (d) and (e). Red colour represent BCC-like phases (ferrite, martensite), while green-coloured areas indicate FCC phase. Black pixels refer to measurement positions with no solutions. The dotted lines in (d) highlight some grain and twin boundaries. (For interpretation of the references to colour in this figure legend, the reader is referred to the Web version of this article.)

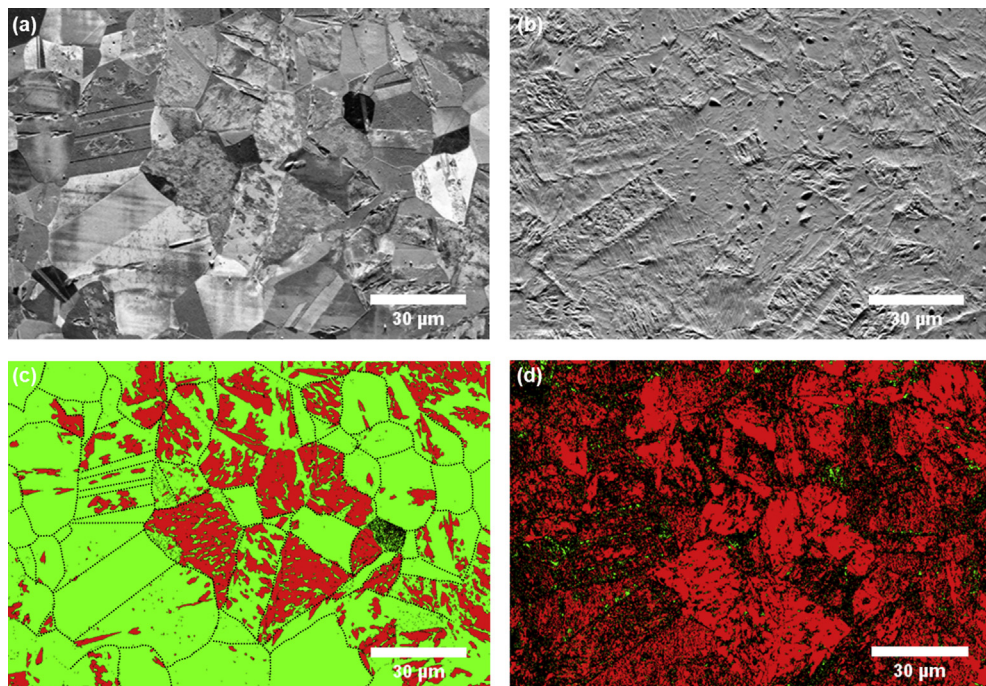


Fig. 3 – SEM images of the investigated steel (a) before and (b) after electrochemical charging for 48 h. (c) and (d) display the respective phase distribution maps collected by EBSD. Red colour represent BCC-like phases (ferrite, martensite), while green-coloured areas indicate FCC phase. Black pixels refer to measurement positions with no solutions. The dotted lines in (c) highlight some grain and twin boundaries. (For interpretation of the references to colour in this figure legend, the reader is referred to the Web version of this article.)

δ -ferrite is an intrinsic part of the investigated alloy. It originates during solidification and depends strongly on the chemical composition of the material [36].

The increased roughness of the surface can be explained by the formation of α' -martensite. This strain-induced transformation of austenite is characterised by a volume increase and shift of the orientation relations of the unit cell which led to a distortion of larger areas of the matrix [37,38]. According to Martin et al. the volumetric expansion is about 2.7% [39]. Calculations by Yang et al. yielded values of 1.5–3.5% [3].

Bullough et al. ascribed the surface relief to a shape deformation. Martensite evolves at the expense of the austenitic parent lattice surrounding it. The shear movement of atomic planes, concomitant with altered orientation relationships of the unit cells and the induced movement of dislocations result in this relief formation [40].

The uptake of atomic deuterium and its accumulation increases the mean lattice plane spacing. Rozenak et al. proved this by XRD measurements on steel AISI 304 observing peak shifts to smaller Bragg angles (bigger lattice plane distances). They derived an increase of 5.8% for γ and 5.5% for ϵ [41–43].

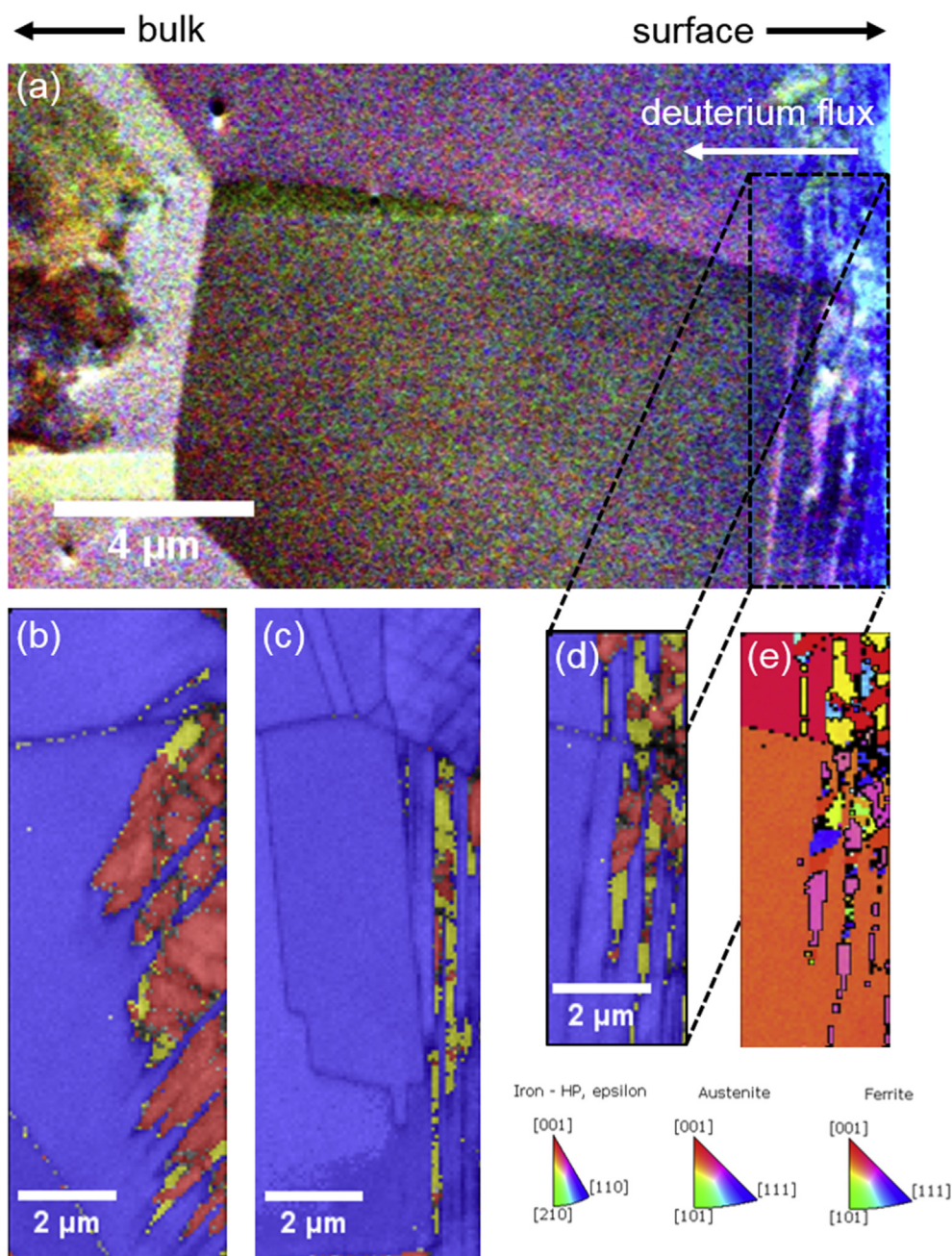


Fig. 4 – (a) SEM image of the cross-section with the corresponding EBSD phase map in (b) and the orientation map in (c). (d) and (e) show other regions of the sample. Red colour represents BCC-like phases (ferrite, martensite), yellow refers to HCP and FCC is indicated by blue colour. The direction of the deuterium ingress is shown by a white arrow. (For interpretation of the references to colour in this figure legend, the reader is referred to the Web version of this article.)

Sobol et al. investigated deuterium-induced effects in duplex stainless steels. SEM and EBSD investigations revealed that blistering exclusively occurred in the ferritic phase [4,28,44]. Similar features are visible in Figs. 2(b) and 3(b) when compared to the phase maps shown in Figs. 2(d) and 3(c). The material's surface shows blisters in the BCT phase, whereby the sample charged for 48 h has a greater number. As reason for blistering an accelerated diffusion of deuterium in martensite combined with a slower diffusion in an austenite grain beneath is assumed. Thus, accumulation of deuterium at the martensite-austenite interface is expected.

The inset in Fig. 2(c) is an image collected at a no-tilted samples in contrast to the image in (a) and (b) which are captured at typical EBSD geometry, i.e. from a 70° tilted sample surface. This enables the observation of surface fissures. Longer cracks mainly appear along grain and twin boundaries, whereas smaller secondary cracks are formed with no defined direction. The crack formation is explained by the electrochemical charging process [3,4,45–48]. According to the internal pressure theory in Ref. [49], deuterium enters the material, accumulates and recombines. As a result of stresses, microcracks are formed at the surface. It is assumed that the concomitant deuterium-induced decrease in cohesive strength of the lattice facilitates this process [47]. An effect described by the HEDE mechanism [?].

According to Wendler et al. [20], austenitic stainless steels with a stacking fault energy (SFE) less than 18–20 mJ/m² tend to martensitic transformation under mechanical load. The calculation of the SFE for the here investigated steel yields values of 15.7–18.1 mJ/m², depending on the equation used [39]. This SFE indicates that a charging-induced $\gamma \rightarrow \epsilon \rightarrow \alpha'$ transformation is at least likely.

The phase distribution maps in Figs. 2(e) and 3(d) prove the assumed transformation from austenite to α' -martensite. No ϵ -martensite was detected. The

comparison between Figs. 2(e) and 3(d) indicates that a higher fraction of austenite in the sample charged for 48 h transformed into martensite which is consecutive since more deuterium can enter the matrix and induce more strain [8,10,50]. The accumulation and assumed recombination to D₂ molecules induced pressure in the matrix providing the driving force for the strain-induced $\gamma \rightarrow \alpha'$ -transformation.

To obtain more insight into the processes of hydrogen- and deuterium-induced phase transformation, cross-sections of the examined samples were produced and analysed with EBSD. The results are shown in Fig. 4 for a sample charged for 24 h and in Fig. 5 for a specimen charged for 48 h.

The SE image in Fig. 4(a) shows a distortion of the lattice in the first 2.5–3 μm of the material. The phase maps in Fig. 4(b)–(d) reveal the partial transformation of the FCC matrix to ϵ - and α' -martensite in that depth range. It is important to point out that the transformation was exclusively located on thin, parallel lines, which can be referred to slip or deformation bands. The EBSD images of the cross-sectioned sample charged for 48 h, shown in Fig. 5, confirm this.

The strain-induced $\gamma \rightarrow \epsilon \rightarrow \alpha'$ -evolution on deformation bands in austenitic stainless steels was suggested by Olson and Cohen [51] and confirmed by several studies, e.g. Refs. [52–55].

The concordance of the present results and the literature strongly supports the theory that deuterium affected the material the same as mechanical loads and therefore induced phase transformations in the investigated steel. Thus, it can be assumed that the uptake and subsequent accumulation and recombination of deuterium built up stress, which caused the formation of stacking faults and plastic deformation. This happened in preferred slip systems with highest Schmid factor μm [53]. Stress concentration within the emerging deformation bands led to $\gamma \rightarrow \epsilon \rightarrow \alpha'$ -transformation.

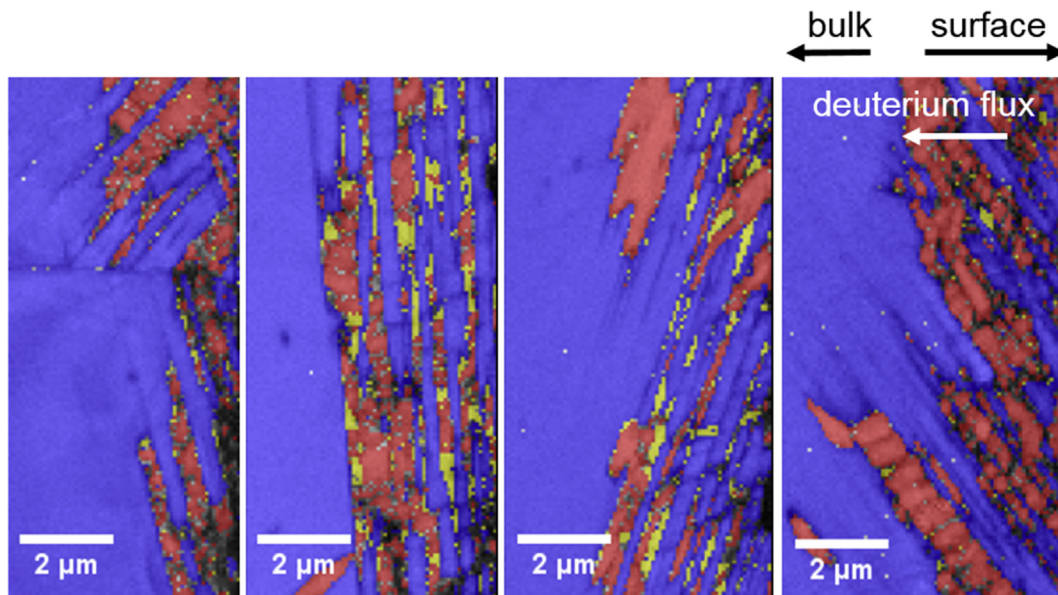


Fig. 5 – EBSD phase maps of different areas of the cross-section. Red colour represents BCC-like phases (ferrite, martensite), yellow refers to HCP and FCC is indicated by blue colour. The direction of the deuterium ingress is shown by a white arrow. (For interpretation of the references to colour in this figure legend, the reader is referred to the Web version of this article.)

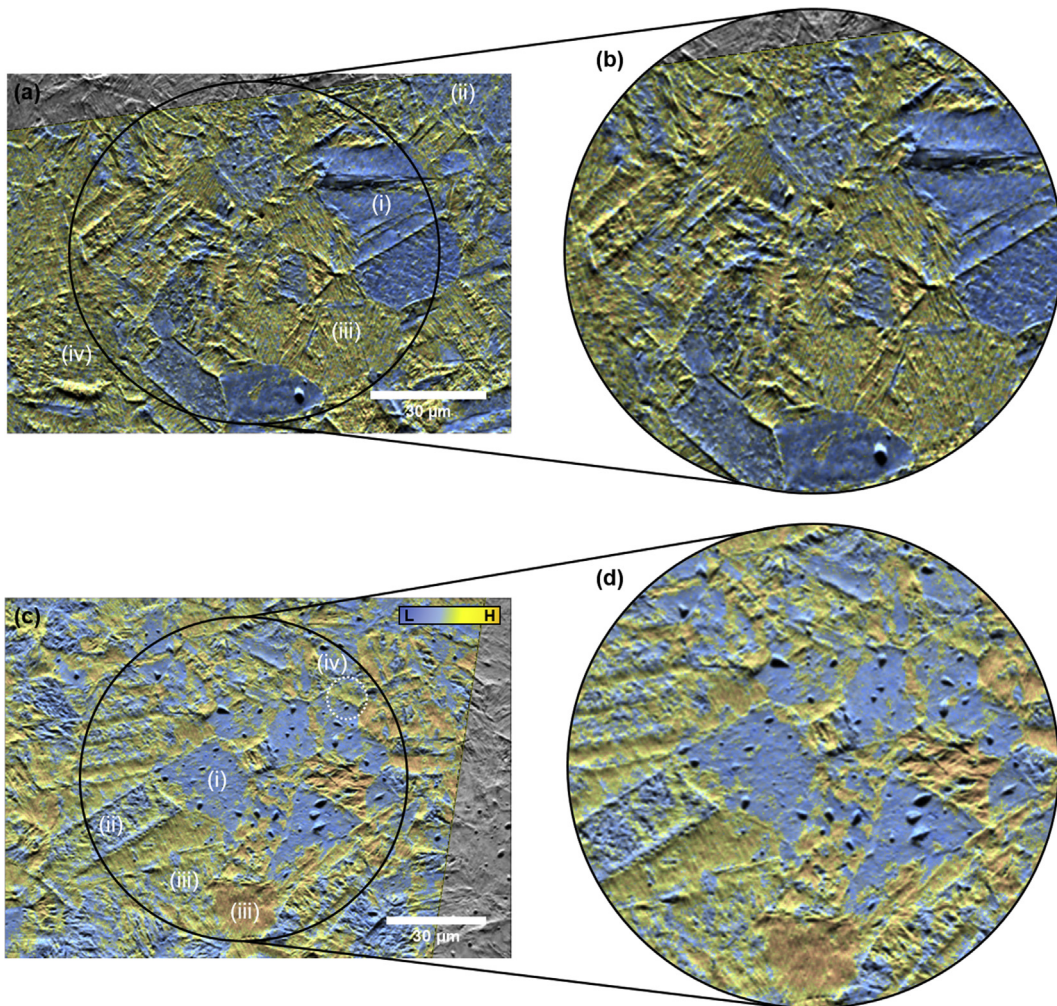


Fig. 6 – Fusion of ToF-SIMS data and SEM images of the sample charged for (a) 24 and (c) 48 h and magnified areas of the same ROIs in (b) and (d). Depicted is the distribution of deuterium and its co-covariants as the PC2 score after principal component. For more information, the reader is referred to the supplemental information. The colour bar represents the signal intensity.

Unlike shown in Figs. 2 and 3, where sample preparation caused entire austenite grains to transform into α' -martensite, in Figs. 4 and 5 only certain areas, which can be referred to as slip bands, changed their crystal structure. The preparation-induced phase transformation would have caused the complete transformation of the cross-section, instead of localised deformation bands. Another indicator is the presence of HCP ϵ -martensite. This phase is the preliminary stage of the $\gamma \rightarrow \epsilon \rightarrow \alpha'$ -transformation. Because it is not stable, it would have transformed completely into BCT martensite, when exposed to the mechanical stress of the diamond-studded wire or polishing. Thus, the preparation of the cross-sections can be excluded as the cause of the martensitic transformation.

The highest stress occurred near the surface because of the higher concentration of deuterium compared to the bulk. Accordingly, the meta-stable ϵ -martensite, which was built from the austenite, transformed completely to α' .

Pan et al. charged AISI 304 austenitic stainless steel with hydrogen and measured its concentration and the amount

of newly formed martensite. They found that higher amounts of hydrogen caused a higher extend of phase transformation and defined a threshold of 30 wt.-ppm under which no $\gamma \rightarrow \epsilon \rightarrow \alpha'$ -transformation occurred [56]. According to this, in the present study it is concluded that the concentration of deuterium at the surface exceeded 30 wt.-ppm both after 24 and 48 h of charging. With increasing depth, the concentration decreased below the threshold and no phase transformation occurred.

Comparing Figs. 4 and 5 qualitatively, differences in the penetration depth of deuterium become visible. In relation, ϵ - and α' -martensite were detected deeper in the material of the sample that was charged for 48 h. This can be expected as diffusion is a time dependent process.

Distribution of deuterium

The results of the PCA and the data fusion of ToF-SIMS and SEM images are shown in Fig. 6.

Deuterium is distributed in the matrix heterogeneously so that different accumulation sites were identified. Ferrite and martensite grains with relatively low deuterium concentration are marked with (i). The low concentration is due to the low solubility and high diffusivity of deuterium in this phase. Thus, atoms could easily diffuse into the grain but were not trapped deeply. It is assumed that after charging stopped, deuterium was effusing from the matrix rapidly.

(ii) Also shows regions with a relatively low amount of deuterium. With comparison to Fig. 2 and 3, it becomes clear that these grains were former austenite which transformed to martensite. The conversion of the lattice structure from FCC to BCT was accompanied by the decrease of solubility and the increase of diffusivity [18,57]. As a consequence, most of the trapped deuterium was released from the grains.

In contrast to this are grains exemplary marked with (iii). These former austenitic grains transformed into martensite as well, but exhibited considerably higher deuterium concentrations. α' -martensite contains many defects like dislocations or stacking faults, which can act as traps for hydrogen/deuterium [18,58]. It is possible that the trapped deuterium, being released during the transformation, was re-trapped at these defects.

As mentioned before, the Cs^+ sputter cycle preceding the analysis had to be considered as another influential factor for phase transformation. For this reason, a series of test measurements were carried out, revealing a sputtering-induced phase transformation even in uncharged specimens at sputter times longer than 2 min.

The necessary energy of the $\gamma \rightarrow \alpha'$ -transformation can not only be provided by the Gibbs free energy $G_{\gamma \rightarrow \alpha'}$ but also by mechanical load W_{mech} applied on the material [20]. Cooling of metastable austenitic steels increases the Gibbs free energy, but decreases austenite stability and stacking fault energy [53]. Therefore, it is anticipated that cooling down the samples in the ToF-SIMS after charging was not sufficient to start the nucleation of martensite. However, the deuterium-induced mechanical strains that were supported by Cs^+ sputtering provided the necessary mechanical driving force for this process. Because of the reduced diffusivity of deuterium at lower temperatures, its effusion from the newly formed α' regions was retarded, thus allowing it to be detected by SIMS.

Following this, it is assumed that grains marked by (ii) transformed during charging, whereas newly formed martensite labelled with (iii) transformed after charging.

The comparison of Fig. 6 with the phase maps in Figs. 2 and 3 reveals grains with FCC structure enriched with deuterium, marked with (iv). As discussed before, austenite has a high solubility for hydrogen in comparison to BCC/BCT phases. That explains the relatively high amount of deuterium in these grains. However, it is possible that the orientation of the grain was unfavourable for the transformation from FCC to BCT structure.

Summary and conclusions

Although the high fugacity, electrochemical charging condition in the present study does not necessarily reflect in-service

conditions of an application-specific counterpart, the investigated steel AISI 304 L is used in other severe conditions in chemical, petrochemical, nuclear, marine and hydrogen production industries. Despite the different availability and uptake of hydrogen, the experiments can reflect the presence of hydrogen and its distribution in the microstructure. Therefore, following conclusions can be drawn from the results:

- ToF-SIMS and microscopical examinations revealed that the recombination poison NaAsO_2 led to coating of the materials surface during charging. This retarded the hydrogen uptake. Higher concentrations of hydrogen were measured with CGHE in samples charged without NaAsO_2 .
- The formation of blisters in BCC grains and severe roughening of the surface in the austenite were observed. Both features arose through the expansion of the lattice due to the (interstitial) solute deuterium and formation of martensite and slip bands. Longer charging times increased the number of blisters.
- EBSD analysis revealed that martensite was formed at the surface of the specimen and in deformation bands under the surface. Those bands were acting as nucleation sites for high-density stacking faults (ϵ -martensite) and α' -martensite. With longer charging times the outreach into the base material increased as well as the amount of transformed austenite at the surface.
- The comparison of SIMS and EBSD data revealed a heterogeneous distribution of deuterium in the material, depending on the crystal structure. Relatively low deuterium concentrations are determined in BCC grains and higher concentrations in FCC grains.
- The fusion of chemical and topographical data suggested that martensitic transformation occurs both during charging and as a result of deuterium-induced stresses and reduced austenite stability due to sample cooling. Further research on this topic has to be done to clearly identify the underlying processes.

Acknowledgements

The authors thank R. Saliwan-Neumann for the EBSD analysis, M. Buchheim, M. Marten and R. Hesse for sample preparation and B. Steffens for the CGHE measurements. A.R. is grateful for the financial support by the BAM MI-Project "ToF-SIMS analysis and imaging of hydrogen assisted cracking phenomena in steels".

Appendix A. Supplementary data

Supplementary data to this article can be found online at <https://doi.org/10.1016/j.ijhydene.2019.03.058>.

REFERENCES

- [1] Lee JA, Lee DH, Seok MY, Baek UB, Lee YH, Nahm SH, Jang JI. Hydrogen-induced toughness drop in weld coarse-grained

- heat-affected zones of linepipe steel. *Mater Char* 2013;82:17–22.
- [2] Rhode M, Steger J, Steppan E, Kannengiesser T. Effect of hydrogen on mechanical properties of heat affected zone of a reactor pressure vessel steel grade. *Weld World* 2016;60(4):623–38.
- [3] Yang Q, Luo JL. Martensite transformation and surface cracking of hydrogen charged and outgassed type 304 stainless steel. *Mater Sci Eng A-Struct* 2000;288(1):75–83.
- [4] Sobol O, Holzlechner G, Nolze G, Wirth T, Eliezer D, Böllinghaus T, Unger WES. Time-of-flight secondary ion mass spectrometry (ToF-SIMS) imaging of deuterium assisted cracking in a 2205 duplex stainless steel microstructure. *Mater Sci Eng A-Struct* 2016.
- [5] Saleh AA, Hejazi D, Gazder AA, Dunne DP, Pereloma EV. Investigation of the effect of electrolytic hydrogen charging of X70 steel: II. microstructural and crystallographic analyses of the formation of hydrogen induced cracks and blisters. *Int J Hydrogen Energy* 2016;41(28):12424–35.
- [6] Glowacka A, Swiatnicki WA. Effect of hydrogen charging on the microstructure of duplex stainless steel. *J Alloy Comp* 2003;356:701–4.
- [7] Robertson IM, Sofronis P, Nagao A, Martin ML, Wang S, Gross DW, Nygren KE. Hydrogen embrittlement understood. *Metall Mater Trans A* 2015;46A(6):2323–41.
- [8] Takai K, Seki J, Homma Y. Observation of trapping sites of hydrogen and deuterium in high-strength steels by using secondary-ion mass-spectrometry. *Mater Trans* 1995;36(9):1134–9.
- [9] Griesche A, Dabah E, Kannengiesser T, Kardjilov N, Hilger A, Manke I. Three-dimensional imaging of hydrogen blister in iron with neutron tomography. *Acta Mater* 2014;78:14–22.
- [10] Turnbull A. Perspectives on hydrogen uptake, diffusion and trapping. *Int J Hydrogen Energy* 2015;40(47):16961–70.
- [11] Béres M, Wu L, Santos LPM, Masoumi M, da Rocha Filho FAM, da Silva CC, de Abreu HFG, Gomes da Silva MJ. Role of lattice strain and texture in hydrogen embrittlement of 18Ni (300) maraging steel. *Int J Hydrogen Energy* 2017;42(21):14786–93.
- [12] Hannula SP, Hanninen H, Tahtinen S. Influence of nitrogen alloying on hydrogen embrittlement in AISI 304-type stainless-steels. *Metall Trans A* 1984;15(12):2205–11.
- [13] Kim YS, Bak SH, Kim SS. Effect of strain-induced martensite on tensile properties and hydrogen embrittlement of 304 stainless steel. *Metall Mater Trans A* 2016;47A(1):222–30.
- [14] Minkovitz E, Eliezer D. TEM study on the formation of microcracks in connection with -martensite. *J Mater Sci Lett* 1982;1(5):192–4.
- [15] Rozenak R, Bergman R. X-ray phase analysis of martensitic transformations in austenitic stainless steels electrochemically charged with hydrogen. *Mater Sci Eng A-Struct* 2006;437(2):366–78.
- [16] Au M. High temperature electrochemical charging of hydrogen and its application in hydrogen embrittlement research. *Mater Sci Eng A-Struct* 2007;454–455:564–9.
- [17] Tsay LW, Yu SC, Huang RT. Effect of austenite instability on the hydrogen-enhanced crack growth of austenitic stainless steels. *Corros Sci* 2007;49(7):2973–84.
- [18] Kim SJ, Yun DW, Suh DW, Kim KY. Electrochemical hydrogen permeation measurement through TRIP steel under loading condition of phase transition. *Electrochim Commun* 2012;24:112–5.
- [19] Betz G, Wehner GK. Sputtering of multicomponent materials, vol. 2. Springer; 1981. p. 1–117. book section 1.
- [20] Wendler M, Weiß A, Krüger L, Mola J, Franke A, Kovalev A, Wolf S. Effect of manganese on microstructure and mechanical properties of cast high alloyed CrMnNi-N steels. *Adv Eng Mater* 2013;15(7):558–65.
- [21] Warrier M, Rai A, Schneider R. A time dependent model to study the effect of surface roughness on reactive-diffusive transport in porous media. *J Nucl Mater* 2009;390–391:203–6.
- [22] Fisher DJ. Hydrogen diffusion in metals: a 30-year retrospective, vol. 167. Trans Tech Publication; 1999.
- [23] Marchi CS, Somerday BP, Robinson SL. Permeability, solubility and diffusivity of hydrogen isotopes in stainless steels at high gas pressures. *Int J Hydrogen Energy* 2007;32(1):100–16.
- [24] Niehuis E, Grehl T, TOF SIMS. Surface analysis by mass spectrometry. Manchester, UK: IM Publications; SurfaceSpectra Ltd.; 2001. p. 753–78. book section Dual Beam Depth Profiling.
- [25] Kubicek M, Holzlechner G, Opitz AK, Larisegger S, Hutter H, Fleig J. A novel ToF-SIMS operation mode for sub 100nm lateral resolution: application and performance. *Appl Surf Sci* 2014;289:407–16.
- [26] Bro R, Smilde AK. Principal component analysis. *Anal Methods-UK* 2014;6(9):2812–31.
- [27] Heller D, ter Veen R, Hagenhoff B, Engelhard C. Hidden information in principal component analysis of ToF-SIMS data: on the use of correlation loadings for the identification of significant signals and structure elucidation. *Surf Interface Anal* 2017;49(10):1028–38.
- [28] Sobol O, Holzlechner G, Holzweber M, Lohninger H, Böllinghaus T, Unger WES. First use of data fusion and multivariate analysis of ToF-SIMS and SEM image data for studying deuterium-assisted degradation processes in duplex steels. *Surf Interface Anal* 2016;48:474–8.
- [29] Dharani HK, Bhadeshia H. Prevention of hydrogen embrittlement in steels. *ISIJ Int* 2016;56(1):24–36.
- [30] Borchers C, Michler T, Pundt A. Effect of hydrogen on the mechanical properties of stainless steels. *Adv Eng Mater* 2008;10(1–2):11–23.
- [31] Dabah E, Kannengiesser T, Mente T, Beyer K, Brauser S. Quantification of hydrogen effective diffusion coefficients and effusion behavior in duplex stainless steel weld metals. *Weld World* 2013;57(4):561–7.
- [32] Robinson SL, Moody NR, Myers SM, Farmer JC, Greulich FA. The effects of current-density and recombination poisons on electrochemical charging of deuterium into an iron-base superalloy. *J Electrochem Soc* 1990;137(5):1391–7.
- [33] Holzlechner G, Kubicek M, Hutter H, Fleig J. A novel ToF-SIMS operation mode for improved accuracy and lateral resolution of oxygen isotope measurements on oxides. *J Anal Atomic Spectrom* 2013;28(7):1080–9.
- [34] Straub F, Böllinghaus T, Unger WES, Mente T. In-situ detection of deuterium in duplex stainless steels by time-of-flight secondary ion mass spectrometry (ToF-SIMS). In: International hydrogen conference (IHC 2012). ASME press; 2014. p. 505–13.
- [35] Michalska J, Labanowski J, Cwiek J. Hydrogen effects in duplex stainless steel welded joints - electrochemical studies. *IOP Conf Ser Mater Sci Eng* 2012;35.
- [36] Fu JW, Yang YS. Origin of the lathy ferrite in AISI 304 stainless steel during directional solidification. *J Alloy Comp* 2013;580:191–4.
- [37] Olden V, Thaulow C, Johnsen R. Modelling of hydrogen diffusion and hydrogen induced cracking in supermartensitic and duplex stainless steels. *Mater Des* 2008;29(10):1934–48.
- [38] Nolze G. Interphase boundary characterization in duplex steel and iron meteorites using EBSD technique. *Arch Metall Mater* 2006;51(1):8.
- [39] Martin S, Wolf S, Martin U, Krüger L, Jahn A. Investigations on martensite formation in CrMnNi-TRIP steels. In: ESOMAT; 2009.

- [40] Bullough R, Bilby BA. Continuous distributions of dislocations - surface dislocations and the crystallography of martensitic transformations. *Proc Phys Soc Lond B* 1956;69(12):1276–86.
- [41] Rozenak P, Eliezer D. Nature of the γ -phase and γ^* -phase in austenitic stainless-steels cathodically charged with hydrogen. *Metall Trans A* 1988;19(3):723–30.
- [42] Rozenak P, Loew A. Stress distributions due to hydrogen concentrations in electrochemically charged and aged austenitic stainless steel. *Corros Sci* 2008;50(11):3021–30.
- [43] Rozenak P. Stress induce martensitic transformations in hydrogen embrittlement of austenitic stainless steels. *Metall Mater Trans A* 2014;45A(1):162–78.
- [44] Sobol O, Nolze G, Saliwan-Neumann R, Eliezer D, Boellinghaus T, Unger WES. Novel approach to image hydrogen distribution and related phase transformation in duplex stainless steels at the sub-micron scale. *Int J Hydrogen Energy* 2017;42(39):25114–20.
- [45] Tiegel MC, Martin ML, Lehmberg AK, Deutges M, Borchers C, Kirchheim R. Crack and blister initiation and growth in purified iron due to hydrogen loading. *Acta Mater* 2016;115:24–34.
- [46] Laureys A, Van den Eeckhout E, Petrov R, Verbeken K. Effect of deformation and charging conditions on crack and blister formation during electrochemical hydrogen charging. *Acta Mater* 2017;127:192–202.
- [47] Pérez Escobar D, Miñambres C, Duprez L, Verbeken K, Verhaege M. Internal and surface damage of multiphase steels and pure iron after electrochemical hydrogen charging. *Corros Sci* 2011;53(10):3166–76.
- [48] Zhang L, Shen H, Lu K, Cao W, Sun Y, Fang Y, Xing Y, Du Y, Lu M. Investigation of hydrogen concentration and hydrogen damage on API X80 steel surface under cathodic overprotection. *Int J Hydrogen Energy* 2017;42(50):29888–96.
- [49] Zapffe CA, Sims CE. Hydrogen embrittlement, internal stress and defects in steel. *T Am I Min Met Eng* 1941;145:225–61.
- [50] Silverstein R, Eliezer D. Hydrogen trapping mechanism of different duplex stainless steels alloys. *J Alloy Comp* 2015;644:280–6.
- [51] Olson GB, Cohen M. Kinetics of strain-induced martensitic nucleation. *Metall Trans A* 1975;6(4):791.
- [52] Weidner A, Martin S, Klemm V, Martin U, Biermann H. Stacking faults in high-alloyed metastable austenitic cast steel observed by electron channelling contrast imaging. *Scripta Mater* 2011;64(6):513–6.
- [53] Biermann H, Solarek J, Weidner A. SEM investigation of high-alloyed austenitic stainless cast steels with varying austenite stability at room temperature and 100°C. *Steel Res Int* 2012;83(6):512–20.
- [54] Linderov M, Segel C, Weidner A, Biermann H, Vinogradov A. Deformation mechanisms in austenitic TRIP/TWIP steels at room and elevated temperature investigated by acoustic emission and scanning electron microscopy. *Mater Sci Eng A-Struct* 2014;597:183–93.
- [55] Weidner A, Segel C, Biermann H. Magnitude of shear of deformation-induced α' -martensite in high-alloy metastable steel. *Mater Lett* 2015;143:155–8.
- [56] Pan C, Chu WY, Li ZB, Liang DT, Su YJ, Gao KW, Qiao LJ. Hydrogen embrittlement induced by atomic hydrogen and hydrogen-induced martensites in type 304L stainless steel. *Mater Sci Eng A-Struct* 2003;351(1–2):293–8.
- [57] Sobol O, Straub F, Wirth T, Holzlechner G, Böllinghaus T, Unger WES. Real time imaging of deuterium in a duplex stainless steel microstructure by time-of-flight SIMS. *Sci Rep-UK* 2016;6:19929.
- [58] Lee SJ, Ronevich JA, Krauss G, Matlock DK. Hydrogen embrittlement of hardened low-carbon sheet steel. *ISIJ Int* 2010;50(2):294–301.